STUDY OF BUOYANCY DRIVEN HEAT TRANSPORT IN SILICONE OILS AND IN LIQUID NITROGEN IN VIEW OF COOLING APPLICATIONS

K. Satpathy[1†], A. Duchesne[2], C. Dubois[2], J.-F. Fagnard[1], H. Caps[2], P. Vanderbemden[1], B. Vanderheyden[1]

[1]Department of Electrical Engineering & Computer Science B28, University of Liège, B-4000 Liège, Belgium

[2]GRASP, UR-CESAM Physics Department B5, University of Liège, B-4000 Liège, Belgium

ABSTRACT

Motivated by applications for cooling superconducting pellets with liquid nitrogen, we consider a source with a fixed heating rate per unit volume, immersed in a liquid pool and cooled through natural convection. In one recent experimental investigation (Dubois et al., Eur. Phys. J. E (2016) 39: 79) carried on silicone oils and liquid nitrogen, we have demonstrated that the velocity field satisfies specific scaling laws with respect to the temperature increase in the liquid pool. In this work, we pursue the analysis by modeling the heat transfer in a parallelepiped enclosure for a steady laminar flow regime. The Navier-Stokes equations are solved using a finite volume approach to obtain the detailed three-dimensional flow and heat-transfer characteristics. A quantitative analysis of the velocity field over the temperature field shows that the experimental power laws are reproduced in simulations. Following Dubois and Berge (J. Fluid. Mech. (1978) 85: 641), a theoretical law originally introduced in the context of the classical Rayleigh-Bénard experiment is shown to be satisfied in the simulations over a wide range of Rayleigh numbers (Ra), assuming the definition of the characteristic convection length is adapted to the investigated geometry. Moreover, the simulations are shown to correctly

reproduce the main features of the flow, including the characteristic convection length, for different heater lengths.

Keywords: *Computational Fluid Dynamics (CFD), Rayleigh Number (Ra), Rayleigh-Bénard convection, convective cooling*

Acknowledgement: This Project has been financially supported by ARC Super Cool contract of the University of Liège under reference *ARC 11/16-03.*

†Correspondence: *ksatpathy@ulg.ac.be*

1.0 INTRODUCTION

High-temperature superconducting materials in the form of single grains of a few cm^3 are capable of trapping magnetic flux densities exceeding those of conventional permanent magnets. Magnetic flux densities in excess of 17 T were trapped in bulk superconductors at temperatures below 30 K [1, 2], and densities up to 3 T were trapped at 77 K [3]. Bulk superconductors are thus very promising materials to be used in electrical systems such as motors, generators, magnetic bearings, and magnetic resonance devices [1, 2].

The design of superconducting applications must include a cryogenic unit. First, the material must be maintained below its critical temperature, T_c, above which it becomes a normal material (typically, $T_c \sim 90$ K for YBCO, so that liquid nitrogen is a genuine cryofluid). Second, under time-varying fields, the material may undergo losses and self-heating, resulting in a reduction of the trapped magnetic flux [4]. To avoid a performance loss, the cryogenic system must then rapidly extract the generated heat and transfer it away from the superconducting material. As a result, it is of great interest to understand the flow and the heat transfer in cooling fluids in the presence of a volumic source with a fixed heat generation rate. Such a situation is also of interest in many practical and industrial applications implying a local heater immersed in a fluid.

As evidenced in our earlier investigation [5], in such a situation, one can expect the buoyancy to be the driving force of the convective flow in the considered device. An extensive bibliography on natural convection in cavities up to 1988 may be found in the review article by Ostrach [6]. The majority of the published studies can be classified into two groups: enclosures heated from below and cooled from above (Rayleigh–Bénard problem) and differentially heated enclosures. More recent literature on this topic show a large interest in the studies of convective phenomena in cavities heated from below and cooled with various boundary conditions [7 - 9].

Towards the effect of fluid properties on the process of heat transfer, Emery and Lee [10] studied the fluid property variations in a square cavity with different boundary conditions on the sidewalls. A comparison was made against constant property and it was observed that the overall heat transfer is unaffected by the variation of the fluid properties, although the flow and temperature fields in the cavity seem to be different. Chu and Hickox [11] studied localized heating in a horizontal enclosure of square platform. In their work, which was complemented by experiments, a constant-temperature heated strip of fixed width was placed on the bottom wall of the enclosure. The effect of horizontal heated strips at the bottom wall of an industrial glass melting tank in two and three-dimensions was studied numerically by Sarris et al. [12]. To improve internal natural convection heat transfer, Ngo and Byon [13] studied the effects of heater location and heater size in a 2D square cavity using a finite element approach. Numerical results indicated that the average Nusselt number increases as the heater size decreases.

Closer to the situation considered in this work, numerous studies focused on the convection induced by a local heater attached on one of the liquid pool walls [14, 15]. Considerable attention has been given to classical Rayleigh-Bénard convection from vertical/horizontal enclosures specified either with constant temperature or heat flux (Öztop et al., [16]). However, a very limited number of studies [17] considered convective heat transfer from a local source, which is specified with a constant volumic heat generation rate and is located away from the liquid pool walls. This situation is different from the classical Rayleigh-Bénard problem where periodic convective cells appear.

This work is focused on the buoyancy driven heat transfer in cooling fluids, in the case of an immersed volumic source with a fixed heat generation rate.

Obtaining accurate measurements, for instance by means of particle imaging velocimetry, may be difficult and is particularly challenging for liquid nitrogen. A well-controlled and uniform temperature must be obtained in the cryostat, as small local temperature variations (0.1 to 1 K) may cause parasitic boiling or evaporation. This condition is particularly difficult to achieve for cryostats where windows using different materials are required to observe the flow. The cryostat enclosure also limits the field of view and thus the size of the region which may be investigated (in commercial cryostats this field of view is typically of a few cm^2).

In this context, we make the choice to focus on a numerical analysis. It comes as a very useful complementary approach, with ideal environmental parameters, where the 3D distribution of both velocity and temperature can be determined over the entire system (which is difficult to achieve experimentally even with a non-cryogenic fluid). Through an analysis of the flow as a function of the physical properties of the liquid and the geometry of the system, numerical simulations also help to understand the underlying physical mechanisms and identify their relevant parameters.

Prior to the present work, we have recently studied numerically the convective flow induced by a heater immersed in a 10 cst silicone oil [18]. It was shown that the characteristics of the flow depend on the length of the heater and that longer heaters lead to lower average Nusselt numbers thereby extending the predictions of [13] to the geometry of an immersed heater.

In parallel, we have studied experimentally the laminar convection flow induced in a similar system with silicone oils and liquid nitrogen, for Rayleigh numbers (Ra) ranging from 10^4 to 10^7 [5]. A flow pattern with two counter-rotating cells, reminiscent of the classical Rayleigh-Bénard cells, was observed. The maximal vertical velocity between the two cells, v_z, was studied as a function of the temperature difference between the heater and the liquid pool,

ΔT, and was found to nearly follow a square root law, as $v_z \sim \Delta T^m$ with $m \sim 0.5$. Moreover, after having adapted the definition of the characteristic wavelength to the studied geometry, the maximum vertical velocity was shown to follow the theoretical law of Normand et al. [19] for silicone oils. Normand's law was originally derived for a system of convection rolls in a container with horizontal dimensions much larger than its height, and for a regime near the onset of the convection instability. In fact, it was found that the law faithfully reproduced the experimental data over a fairly large range of Rayleigh numbers, including regimes far from the instability threshold. Both these findings and the new definition of the characteristic wavelength shed light on the mechanisms underlying the convective flows which are relevant for engineering cooling applications.

The purpose of this paper is to further analyze the characteristics of the convective flow away from the convection threshold, by means of a 3D numerical model and as a function of the fluid properties and the heater geometry. More specifically, we are seeking to determine whether the velocity-temperature correlations observed in [5] are satisfied in the simulations. Simulation results for different heater lengths are also compared to new data acquired with the same experimental setup.

The paper is organized as follows: The experimental and the modelling methodologies are discussed in Section 2. Fluid flow characteristics inside the domain are presented in Section 3. The discussion is reinforced through an analysis on different coolants (liquid nitrogen, silicon oils) and a comparison with the experimental data. More specifically, the relevance of defining a new characteristic wavelength for analyzing the maximum velocity as a function of the Rayleigh number is confirmed. The convection flow is also investigated for different heater lengths both experimentally and numerically, and it is shown that the predicted characteristic

wavelength is consistent with the measured one. Finally, a summary and conclusions are presented in Section 4.

2.0. EXPERIMENTAL PROCEDURE AND SOLUTION METHODOLOGY

2.1 Investigated Fluids

In both the experimental and numerical investigations, several cooling fluids are considered in order to cover a wide range of physical properties: silicone oils (0.65, 10, and 20 cst), and liquid nitrogen. Their properties are summarized in Table 1.

2.2. Experimental Procedure

The experimental setup consists in an electrical resistor which is fed with an electrical current and acts as a heating source through Joule dissipation. The heater is immersed in a liquid pool of volume 200 x 100 x 30 mm^3 at a distance of several tens of mm below the liquid free surface. The flow is visualized using a commercial particle imaging velocimetry (PIV) system which records the position of tracers over time and allows the velocity field to be calculated from differences between two successive images. The detailed description of the setup, the PIV markers, the laser source, and the velocity calculations can be found in Ref. [5]. Three different resistors are considered in this work: a short rectangular heater of 6 x 3 x 1 mm^3, and two long wire heaters of length of 5.7 cm and 10.1 cm, respectively. For reader's perspective; the thermalization of the experimental set-up has been expressed in the appendix A of the manuscript (see page 29).

2.3. Numerical Model: Governing Equations and Fluid Properties

The three-dimensional incompressible steady forms of Navier-Stokes equations are solved for obtaining the fluid flow and heat transfer characteristics in a parallelepiped cavity. The governing equations in the cartesian coordinates system are given as [20]:

Continuity: $$\frac{\partial u}{\partial x}+\frac{\partial v}{\partial x}+\frac{\partial w}{\partial z}=0 \quad (1)$$

x-momentum: $$u\frac{\partial u}{\partial x}+v\frac{\partial u}{\partial y}+w\frac{\partial u}{\partial z}=\frac{-1\partial p}{\rho\ \partial x}+\nu\left(\frac{\partial^2 u}{\partial x^2}+\frac{\partial^2 u}{\partial y^2}+\frac{\partial^2 u}{\partial z^2}\right) \quad (2)$$

y-momentum: $$u\frac{\partial v}{\partial x}+v\frac{\partial v}{\partial y}+w\frac{\partial u}{\partial z}=\frac{-1\partial p}{\rho\ \partial y}+\nu\left(\frac{\partial^2 v}{\partial x^2}+\frac{\partial^2 v}{\partial y^2}+\frac{\partial^2 v}{\partial z^2}\right)+g\beta\left(T-T_0\right) \quad (3)$$

z-momentum: $$u\frac{\partial w}{\partial x}+v\frac{\partial w}{\partial y}+w\frac{\partial w}{\partial z}=\frac{-1\partial p}{\rho\ \partial z}+\nu\left(\frac{\partial^2 w}{\partial x^2}+\frac{\partial^2 w}{\partial y^2}+\frac{\partial^2 w}{\partial z^2}\right) \quad (4)$$

energy: $$u\frac{\partial T}{\partial x}+v\frac{\partial T}{\partial y}+w\frac{\partial T}{\partial z}=\alpha\left(\frac{\partial^2 T}{\partial x^2}+\frac{\partial^2 T}{\partial y^2}+\frac{\partial^2 T}{\partial z^2}\right)+q'' \quad (5)$$

Here, the flow model is based on the assumptions that the fluid is Newtonian and laminar. The fluid properties are constant with the exception of the density in the body force term of the momentum equation. The Boussinesq approximation [21] is invoked for the fluid properties to relate density changes to the temperature of the flow field. (See the third term of the right side of (3), where T is the local temperature, T_0 is the temperature of the liquid at rest, and ρ is the fluid density at T_0). *u, v,* and *w* refer to the rectangular velocity components of the velocity vector *U=(u,v,w)*, *p* is the pressure relative to the hydrostatic pressure, and gravity (*g*) is acting along the negative *y*-axis. (q″) represents the uniform heat generated inside the heater surface ($Q/\rho C_p$) and Q is the volumetric heat source. β, ν and α are the thermal expansion coefficient, kinematic viscosity and thermal diffusivity respectively. The flow characterized by the Rayleigh Number

$$Ra = g\beta\Delta TL^3/\nu\alpha, \quad (6)$$

where ΔT ($T_h - T_0$) is the maximum temperature difference measured across the liquid pool, L is the liquid height above the heater (see Fig. 1). For the cooling liquids listed in Table 1, the range of investigated Rayleigh numbers is [3×10^5 - 2×10^8]. Towards defining the Rayleigh number, we took the liquid pool height as the characteristic length scale, while other authors oftentimes refer to the length of the cavity/heater [13]. This choice is motivated by the fact that we are seeking to compare the results in the present geometry to those obtained in the classical Rayleigh-Bénard experiment, as will be discussed in detail in Sec. 3.4.4.

The simulations are carried out in the convection regime with $Ra > Ra_c$, where Ra_c is the convection threshold (Ra_c = 1707 for rigid-rigid boundary conditions, [22]). The flow is modelled as steady, laminar, and non-turbulent, an assumption which clearly holds for $Ra \leq 2\times10^7$. Although the range of investigated Ra extends to 2×10^8, where turbulence is likely to start playing a role (the transition to turbulence is beyond the scope of the present research), it will be shown that the simulation results based on convection alone are still reproducing the experimentally observed correlations. Last, note that the surface tension effects associated with the Marangoni-Bénard instability can be neglected as the Bond number is larger than 150, see Ref. [5].

2.4. Numerical Model: Domain Geometry and the Boundary Conditions

Taking domain symmetry into account, only half of the liquid pool is modeled to save the computation time. The computational domain is taken as a rectangular parallelepiped with a length (x), height (y) and width (z) of 100 mm, 100 mm, and 30 mm, respectively, see Fig.1. In parallel to experiments, three different heater sources are considered: the short rectangular resistor of 6 mm long, and the wire heaters of 5.7 cm and 10.1 cm, located in each case at 30

mm below the liquid free surface and placed symmetrically with respect to the x = 0 plane. Copper (Cu) is used as the heater medium. The heater Biot number (*Bi*) --- the ratio hL_c/k, where h is the average heat transfer coefficient, L_c is a characteristic length of the heater, and k is the heater thermal conductivity --- is smaller than 0.02. The heater temperature is therefore nearly uniform and very weakly dependent on the heater thermal properties. In turn, the characteristics of the convection flow will essentially depend on the source heating rate.

The boundary conditions are as follows:

- side walls (except top surface and the wall attached to heater surface): no-slip velocity i.e., u(x, y, z) = 0, v(x, y, z) = 0, w(x, y, z) = 0 and zero heat flux conditions $\left(\frac{\partial T}{\partial x}, \frac{\partial T}{\partial y}, \frac{\partial T}{\partial z}\right) = 0$ are imposed;

- wall attached to the heater surface: symmetry $\left(\partial_n[U,T] = 0\right)$ boundary condition i.e., all the normal components of velocity as well as the temperature are zero on the surface (no flux across the boundary), here U = U(u, v, w);

- Top surface (unfilled part as shown in the Fig. 1): $T=T_0$, constant temperature is assumed on the top surface with a free-slip velocity condition (shear stress on the wall $\tau_{wall} = 0$);

- a constant volumic heat generation rate ($q'' = Q/\rho C_p$) is specified for the heater.

We have the feeling that by providing dimensionful equations, we avoid confusion about the reference length and also state our results in an explicit way, so as to facilitate future comparisons to our work. For reader's perspective, the non-dimensional form of the governing equations has been included in the revised manuscript (see appendix B, page 30).

2.5. Numerical Approach

The governing equations (1-5) are solved by a finite-volume method using a general purpose computational fluid dynamics (CFD) software [23]. The pressure-velocity coupling between

the incompressible Navier-Stokes and the continuity equations are solved using the SIMPLE algorithm [24]. The first-order upwind scheme is chosen for the spatial discretization. To check the convergence of the solution, an error (ε) in the discretized momentum and energy equations is set using a tolerance criterion as $\varepsilon \leq 10^{-5}$ and 10^{-10}. Further details related to the flow solver and the spatial discretization scheme are available in [23]. Since, the geometry is unusual and probably more stable in terms of induced flow than the classical Rayleigh–Bénard experiment (as will be seen below, the fluid can flow around the heater sides) no temporal oscillations were observed in our in-house experiment, which adds further values for choosing the steady state simulations.

3.0. RESULTS AND DISCUSSION

3.1 Benchmark Validation

In the present investigation, the emphasis is on the flow features and the heat transfer analysis between the local heater and the surrounding cooling liquids. Towards this, buoyancy driven flow in an enclosed cavity [25] forms a good test case for the present validation. This particular benchmark analysis was successfully investigated in our earlier studies in a 2D geometry [18]. A comparison was made between the velocity and temperature (stream functions) distributions inside the cavity obtained in the present analysis and the test case of Ref. [25]. The heat transfer characteristics along the heated surface was evaluated in terms of the average Nusselt number for a wide range of Rayleigh numbers ($Ra = 10^3$ - 10^5) with a fixed Prandtl number ($Pr = 0.7$). Overall, a satisfactory agreement was found between the present simulations and the benchmark results.

3.2. Mesh Sensitivity Analysis

Establishing the optimal mesh size towards independent nature of the solution is an essential first step in the numerical simulation. It is observed that the grid distribution from the heater

surface is important towards resolving the large temperature gradient across the solid-fluid interface. Towards this, the grid refinement near the heater surface is done by using a size function (boundary layer) with a growth factor of 1.1. The nearest element from the heater surface is located at a distance of 0.6 mm and varies from coarse (M1) to refined mesh (M3). Also, the volume mesh is refined accordingly to avoid the computational divergence. The different mesh sizes in terms of volume (control volumes) and boundary layer mesh employed for the 3D numerical analysis are listed in Table 2. It can be noticed that the relative changes in the computed temperature difference ΔT (across the system) and the maximum vertical velocity above the heater surface are small (< 10 %) when going from mesh M2 – M3, whereas the computational cost increases substantially. Thus, mesh M2 is chosen as the optimized grid for the preceding simulation. As discussed in more details below, the observed difference between the numerical result (velocity magnitude) and the experiment is likely due to an averaging e□ect, as PIV velocities are calculated from the flow time-lapse over small regions of space. Despite this, the agreement on the flow and thermal behavior between the experiments and simulations is satisfactory.

3.3 Qualitative characteristics of the flow and comparison to experiments.

We now turn to compare the flow observed in liquid nitrogen for a 6 mm heater dissipating 40 mW to that obtained from the numerical model. The computations were carried in a full 3D geometry, whereas the PIV experiments gave measurements in the yz plane. In order to facilitate the comparison with experiments, we are thus presenting the results in the yz plane, cut across the 3D domain, and complete the data with visualization of the flow in the perpendicular xy plane.

Figure 2 depicts the close-up view of vertical velocity distributions above the heater surface in the yz plane. For reader's perspective, we have used the same scale for a fair

comparison with the experiment (PIV), but the numerical value of the velocity magnitude is higher in the simulations. The differences observed between the laminar calculations and the PIV measurements is most likely due to experimental uncertainties. The typical error bars, reported by Dubois et al., [5] appears to be non-negligible, due to a limited spatial resolution. The flow has to be tracked over a large window with enough parcels and is then averaged over cells of typical size of 1.2 x 1.2 mm^2. As a result of this averaging procedure, the velocities in the central region (where the flow is the fastest) are in fact underestimated. In addition, the field of view has a certain depth, resulting in an error on the position in the (yz) plane of about 1 mm and a further averaging. Moreover, one cannot totally eliminate small thermal defects on the wall that create parasite flows. Despite these multiple sources of discrepancy, the overall agreement between the experiments and the simulations is rather good regarding the velocity field distribution, the vortex core position and the width of the thermal plume.

Figure 3 shows a typical steady state flow pattern in the form of path lines colored by individual particle (plane $z = 0$). By contrast to PIV experiments which probe the velocity field in a limited region, the simulated flow is obtained over the entire domain. Simulations thus yield pieces of information which are out of reach experimentally. The maximum vertical velocity occurs above the heater, along the axis with $x = 0$ and $z = 0$. The flow just above the heater ascends towards the cold free surface, then moves horizontally towards the top corner of the tank, descends to the bottom of the cavity and finally returns to the heated region. Here, as shown in Fig. 3, the circulations appearing in the cavity are lifted up, with their cores closer to the top wall (cold wall). This is due to the dominance of the convection over conduction (high value of average Nusselt number). The maximum vertical velocity occurs close to the top surface due to action of buoyancy, as expected. Below the heater, the flow is not as much affected as that above the heater and remains stagnant due to the no-slip conditions. Flow

acceleration occurs along the container the side walls due to gravity, which eventually generates a large convective cell in the upper part of the tank.

The temperature fields shown in Fig. 4 (same modeled area as Fig. 3) reveal the existence of two separate regions, a cold uniform temperature region and a hot region. The top surface, the sidewall and the part of the bottom wall not covered by the heater have almost the same (low) temperature whereas the temperature gradients are concentrated just above the heater, where a thermal plume is formed. The rising fluid in the thermal plume will have to return to the bottom to replace that already risen, resulting in a recirculation pattern. A gradual variation of the static pressure distribution is found, evolving from maximum at the bottom to minimum at the top. The velocity distribution is calculated in the symmetry plane along the line $x = 0$ and $z = 0$, from the heater surface to the top surface. Figure 5 shows the distribution of velocities, normalized to their maximum values, for both the simulations and the experiment. A line which is one cell away from the symmetry plane and above the heater surface is chosen. The ratio of the velocity plotted along the line to the maximum velocity along the same line gives the normalized velocity. The position of maxima occurs near to the top surface as seen in Fig. 5. The scatter in the experimental data suggests a 5 to 10 % uncertainty in the measured velocities. Despite of this fact, the velocity profiles are in very good agreement. To complete the analysis of the flow structure, the flow profile as viewed from the symmetry plane (yz) (or, $x = 0$) is presented in Fig. 6. A flow bypass occurs along both sides of the heater, resulting in two symmetric convection cells.

3.4. Comparative Studies

3.4.1. 3D versus 2D studies

Prior to analyzing the problem in three dimensions, an attempt was made to understand it in a simple two-dimensional geometry, in order to reduce the complexity and the computational

cost of the model. The heater width in the span wise direction (*z*-axis) is now assumed to be infinitely long. Figure 7 represents the velocity and static temperature profiles for the 2D studies. It is observed that, the nature of the flow features (velocity, temperature, etc.) remains the same as those found in the 3D analysis. Further analysis on the heater lengths indicates that the 2D analysis agrees well with the 3D results for short heater lengths. However, we showed in [19] that for heater lengths of a fraction of the container length, flow features as well as heat transfer characteristics drastically change. Hence, 3D analysis is more realistic for the present scenario and is further discussed in the following sections.

3.4.2. Usage of different Coolants

We now turn to analyze the cooling mechanisms further and investigate the flow pattern over a large range of Rayleigh numbers, from 3×10^5 to 2×10^8, by considering the different cooling fluids listed in Table 1. Figure 8 compares the velocity distribution in the yz plane (or x = 0) and xy plane (or z = 0) for liquid nitrogen and 10cst silicone oil under comparable heating conditions. In both cases, two symmetric convective cells appear around the symmetry axis. However, the cell size is rather small and appears near the top surface for liquid nitrogen (Fig. 8a, left). For silicone oil, which is heavier, the cell is shifted to a lower level and has a larger size (it spans the space between the heater and the top surface) as seen from Fig. 8 (b, right). This larger size may be interpreted as an effect of the viscosity difference between the considered liquids. Indeed, if the thermal conductivity is quite the same between the two liquids, the viscous friction around the ascending flow may be responsible of a larger plume. Furthermore, the velocity distribution along the xy plane for 10 cst silicon oil is compared against the PIV (Fig. 9), with a heating source of 9.79 x 10^5 W/m^3. A very good agreement is observed between the numerical results against the PIV measurement.

Figure 10 shows the maximum vertical velocities above the heater surface for all liquids, plotted as a function of the maximum temperature difference across the domain (ΔT). It is observed that, at a fixed ΔT, the velocity is the highest for the lightest fluid i.e., liquid nitrogen. A fit to the data reveals that each curve follows a power law, as depicted in Fig. 10, with $V_y \sim (\Delta T)^m$, where the values of the exponent '*m*' are listed in Table 3. They range from 0.4 to 0.6 and are in rather good agreement with the experimentally determined exponents.

Note that the simulated data for liquid nitrogen is generated up to $\Delta T = 2K$, corresponding to $Ra = 2\times10^8$, where the flow may start exhibiting turbulence. Remarkably, despite the neglect of turbulence in simulations, the determined exponent is very close to the experimental result.

The non-dimensional temperature distribution for a given power density (2.2×10^6 W/m^3) along a line (same line as defined for the normalized velocity, see page 14, para 2) and, above the heater surface is depicted in Fig. 11. Since, the temperature distribution along the heater surface is almost uniform, hence the temperature gradient is evaluated across the liquid pool height (L). It shows that, the heat transfer rate is maximum across the heater-fluid interface.

3.4.3. Extended heater lengths

We now turn to a study of the effect of the heater length on the fluid flow and seek to identify a convection length which we compare to experimental data. In a first analysis, a heater of 10.1 cm length (Fig. 12a) is considered in a pool of 20cst oil subjected to two different heating powers, of respectively 0.11 W and 0.61 W. The pathline profiles in the xy plane are compared with the PIV measurements, as shown in Fig.12(b).

With respect to Fig. 3, the flow patterns are not significantly affected by the increase in the heater length, but the velocity magnitude decreases. The maximum velocity will be observed in a region away from the symmetry plane (large unfilled white circle in Fig. 12(b), bottom). In this scenario, the flow is drawn inwards from the edge of the heated strip forming boundary layers along its surface which may meet somewhat far from the symmetry wall before they turn through a right angle and form a circulation. As a result, a typical 'anvil' shape with a large region of upward flow is found above the heater. As the heater length increases, the flow tries to confine itself in the space between the heater and the sidewall, a behavior which differs from that of 2D studies (Bénard cell appears close to the symmetry plane for all the cases, [25]). When input powers increase, the cell center appears to move toward the heater surface (marked as small white filled circle). Figure 13(a) depicts the computational domain for 5.7 cm heater length. To proceed with the analysis, we define the length characterizing the convective flow, λ_c, as the distance between the two stagnation points (zero vorticity, marked as black circle in Fig. 13b).

Considering now the three types of heaters (the 6 mm, 5.7 cm, and 10.1 cm long heaters), the correlation between λ_c and the heater length, L_g, was investigated for different input powers. A close agreement between the present analysis and the experiment is observed, as seen from Figs. 14 (a) and (b).

Figure 15 shows how the correlation between the measured vertical velocity and the maximum temperature difference ΔT is affected by the heater length. For silicon oil with a viscosity of 20 cst, the numerical and the experimental data globally gather around a single curve, showing a close agreement as well as a relative insensitivity of the maximum velocity with respect to the heater length. The velocity follows again a power law $V_y \sim \Delta T^m$, with m = 0.6.

3.4.4. Velocity correlations

We now wish to compare the simulated velocity fields against the theory of convection flow. Since, the sidewalls play an important role for large heater lengths (the heater size is of the same order of magnitude as the cavity dimension (x)), we chose the smallest heater to compare with the theory, minimizing the wall effects. Also, we saw in the previous section that the flow pattern varies with the heater length, and resemble more closely the classical Rayleigh-Bénard pattern for the shortest heater lengths. Thus, a heater length of 6 mm is considered. We seek to compare the simulated maximum vertical velocity V_y to the theoretical law given by Normand et al., [19], which was originally established close to the convection instability threshold for a flow bounded by two parallel plates. Defining the distance from the instability onset as $(Ra-Ra_c)/Ra_c$, it was shown that the maximum vertical velocity, V_y, is given as

$$V_y = 1.24\left(\frac{2\pi L}{\lambda_c}\right)^2 \frac{\alpha}{L}\left(\frac{Ra - Ra_c}{Ra_c}\right)^{0.5} \qquad (7)$$

where λ_c is the spatial periodicity of the flow (distance between two adjacent rolls), and α is the thermal diffusivity. The prefactor depends on the imposed boundary conditions; in Ref. [19], rigid wall boundary conditions were imposed on the parallel plates with $Ra_c = 1707$. Here, the heater geometry is di□erent and the walls are not perfect. The latter shifts the instability appearance but has small e□ect as long as the horizontal to vertical ratio is large ($\sim$ 10) [26, 27], which is the case here. Since, our setup did not allow us to accurately measure this threshold, we kept the cited value $Ra_c = 1707$ as the threshold reference. Also, the geometry dependence can probably explain why our results seem to follow Normand's law with a different prefactor than predicted from theory, for the classical parallel plate setup. The present geometry has a heater length of 6 mm, modeled with a volumic source of fixed heating rate in

a three-dimensional cavity with the boundary conditions specified in Sec. 2.2. Under these conditions, convection begins in the form of two regular cells, appearing above the heater (Fig. 16).

The simulated maximum velocity is plotted against the non-dimensional parameter as shown in Fig. 17. The maximum velocity is found to scale with the deviation $(Ra-Ra_c)/Ra_c$ as $V_y \sim ((Ra-Ra_c)/Ra_c)^m$, with m = 0.42 for 20cst oil, m = 0.52 for 10cst and 0.65 cst oils, and m = 0.4 for liquid nitrogen. When all data points are gathered in a single plot, the model of Eq. (7) appears to fit quite well with m= 0.5, however with a smaller prefactor (0.82 instead of 1.24). Note that the fit extends over a large range of Rayleigh numbers, i.e. in situations which might be far away from the convection instability onset. To illustrate this fact, it is interesting to remind that in the early works about natural convection [28], the authors pointed out that, surprisingly, the power law stands for $(Ra-Ra_c)/Ra_c \sim 10$. In fact, the proposed model seems to be relevant over the much larger range $Ra \sim 3\times10^5 - 2\times10^8$, i.e. $(Ra - Ra_c)/Ra_c$ from 2×10^2 to 2×10^5, covering laminar convective flow below and near the onset of turbulence [29, 30].

4.0. SUMMARY AND CONCLUSIONS

In this paper, we investigated the flow induced by a local heat source immersed in a liquid pool and compared our findings with experimental data. The continuity, momentum, and energy equations were solved through a finite-volume approach using a commercial CFD software. Detailed flow and heat transfer characteristics were presented through isotherm contours, velocity vectors, and path line profiles.

Overall, a characteristic 3D flow was observed, exhibiting a flow bypass along the lateral sides of the heater, and resulting in two symmetric convective cells which are reminiscent to, but different from, the classical Rayleigh–Bénard convection pattern. Investigating different silicone oils and liquid nitrogen under different heating conditions, we demonstrated that the maximum vertical velocity increases with the maximum temperature difference as a power law, with an exponent which is in a very good agreement with experiments. Moreover, the general structure of the flow, and its associated characteristic convection length, appears to be faithfully reproduced by the simulations, including in situations where the heater length is increased and the flow pattern changes its structure near the top surface of the heater. For the shortest heater, for which the flow structure is the closest to the classical Rayleigh-Bénard cells, a theoretical law established forty years ago near the convection threshold was found to be satisfied over the very large range of Rayleigh numbers [3×10^5 - 2×10^8], thereby confirming the experimental observations of Ref. [5]. Despite the fact that turbulence may play a role (threshold to turbulence transition is beyond the scope of the present research) in the investigated flows with the highest Rayleigh numbers, the laminar convection simulations are in good agreement with experiments.

REFERENCE

[1] M. Tomita, M. Murakami, High-temperature superconductor bulk magnets that can trap magnetic fields of over 17 tesla at 29 K, *Nature* 421 (2003) 517.

[2] J.H. Durell et al., A trapped field of 17.6 T in melt-processed, bulk Gd-Ba-Cu-O reinforced with shrink-fit steel, *Supercond. Sci. Technol.* 27 (2014) 082001.

[3] S. Nariki, N. Sakai, M. Murakami, Melt-processed Gd-Ba-Cu-O superconductor with trapped field of 3 T at 77 K, *Supercond. Sci. Technol.* 18 (2004) S126.

[4] P. Laurent, J.F. Fagnard, N. Hari Babu, D.A. Cardwell, B. Vanderheyden, P. Vanderbemden, Self-heating of bulk high temperature superconductors of finite height subjected to a large alternating magnetic field, *Supercond. Sci. Technol.* 23 (2010) 124004.

[5] C. Dubois, A. Duchesne, B. Vanderheyden, P. Vanderbemden, H. Caps, Locally induced laminar convection in liquid nitrogen and silicone oils, *Eur. Phys. J. E*39 (2016) 79.

[6] S. Ostrach, Natural convection in enclosures, *J. Heat Transfer* 110 (1988) 1175.

[7] K.E. Torrance, J.A. Rockett, Numerical study of natural convection in an enclosure with localized heating from below-creeping glow to the onset of laminar instability, *J. Fluid Mech*. 36 (1969) 33.

[8] S. Pretot, B. Zeghmati, G.L.Palec, Theoretical and experimental study of natural convection on a horizontal plate, *Appl. Thermal Eng*. 20 (2000) 873.

[9] I. Sezai, A.A. Mohamad, Natural convection from a discrete heat source on the bottom of a horizontal enclosure, *Int. J. Heat Mass Transfer* 43 (2000) 2257.

[10] A.F. Emery, J.W. Lee, The effects of property variations on natural convection in a square enclosure, *ASME J. Heat Transfer* 121 (1999) 57.

[11] T.Y. Chu, C.E. Hickox, Thermal convection with large viscosity variation in an enclosure with localized heating, *ASME J. Heat Transfer* 112(1990) 388.

[12] I.E. Sarris, I. Lekakis, N.S. Vlachos, Glass melt recirculation controlled by a heated strip in the tank bottom, *Proc. of 1st Balkan Conference on Glass*, Volos, Greece (2000) 379.

[13] I. Ngo, C. Byon, Effects of heater location and heater size on the natural convection heat transfer in a square cavity using finite element method, *J. of Mech. Science and Tech*. 29 (7) (2015) 2995.

[14] N. Katsavos, I. Pappa, I. Lekakis, I.E. Sarris and N.S. Vlachos, Study of natural convection from a heating line source of a high Prandtl number fluid in a rectangular cavity, *5th World Conf. on Experimental Heat Transfer, Fluid Dynamics and Thermodynamics*, Thessaloniki, Greece (2001) 591.

[15] B. Gebhart, Y. Jaluria, R.L. Mahajan, B. Sammakia, Buoyancy-Induced Flows and Transport, Springer, 1988.

[16] H. F. Öztop, P. Estellé, W.M. Yan, K. Al-Salem, J. Orfi, O. Mahian, A brief review of natural convection in enclosures under localized heating with and without nanofluids, *Int. Commu. in Heat and Mass Transfer* 60 (2015) 37.

[17] M.Y. Ha and M.J. Jung, A numerical study on three-dimensional conjugate heat transfer of natural convection and conduction in a differentially heated cubic enclosure with a heat-generating cubic conducting body, *Int. J. of Heat and Mass Transfer* 43 (2000) 4229.

[18] K. Satpathy, C. Dubois, A. Duchesne, J.-F. Fagnard, H. Caps, P. Vanderbemden, B. Vanderheyden, Studies on convective cooling of cryogenic fluids towards superconducting applications, *Proc. in Advances in Fluid Mechanics*, Ancona, Italy, (2016).

[19] C. Normand, Y. Pomeau, M.G. Velarde, Convective instability: A physicist's approach, *Rev. of Modern Physics,* 49 (1977) 581.

[20] Y. *Cengel, Heat Transfer*-A Practical Approach, 2nd Edition, McGraw-Hill, *2003.*

[21] J. Boussinesq, Théorie analytique de la chaleur, Gauthier-Villars, Paris, 2, 1903.

[22] A. Pellew, R. Southwell, On maintained convective motion in a fluid heated from below Proc. R. Soc. London A: Math. Phys. Engg. Sci. 176 (1940) 312.

[23] ANSYS 15, User Guide, Ansys, Inc., Lebanon, US, 2012.

[24] S.V. Patankar, Numerical heat transfer and fluid flow, Hemisphere Publishing Corporation, Washington DC, 1980.

[25] G.D. Vahl Davis, Natural convection of air in a square cavity - a benchmark solution, *Int. J. Numer. Meth. Fluids* 3 (1983) 249.

[26] D.K. Catton, J. Edwards, Effect of side walls on natural convection between horizontal plates heated from below, J. Heat Transfer, 89 (1967) 295.

[27] W.L. Heitz, J.W. Westwater, Critical Rayleigh numbers for natural convection of water confined in square cells with l/d from 0.5 to 8, J. Heat Transfer, 93 (1971) 188. [26]

[28] M. Dubois, P. Berge, Experimental study of the velocity field in Rayleigh-Bénard convection, J. Fluid Mechanics 85 (1978) 641.

[29] X. Chavanne, F. Chilla, B. Chabaud, B. Castaing, B. Hebral, Turbulent Rayleigh–Bénard convection in gaseous and liquid He, Phys. of Fluids 13 (2001) 1300.

[30] J.J. Niemela, L. Skrbek, K.R. Sreenivasan, R.J. Donnelly, Turbulent convection at very high Rayleigh numbers, *Nature* 404 (2000) 837.

Table Caption:

1. Fluid properties: kinematic viscosity v, density ρ, thermal expansion coefficient β, thermal diffusivity α, thermal conductivity K_f.

2. Mesh Sensitivity Study for liquid nitrogen subjected to a 6 mm heater dissipating 2.2×10^6 W/m^3 (40 mW).

3. Comparison of the exponent '*m*' for different fluids.

Figure Caption:

1. Schematics of the simulated domain.

2. Close-up view of the flow above the heater surface for the case of liquid nitrogen with a source of power density of 2.2 x 10^6 W/m^3; left: PIV measurement; right: present study for mesh M2. It is noted that, the absence of the velocity vectors in the middle of the present study reflects the regime of higher velocity up to 22 mm/s.

3. Path lines colored by individual particle on the mid plane (z = 0), under the same conditions as in Fig. 2 (see above). The fluid is rising above the heater and descends along the container vertical wall.

4. Distribution of the temperature difference T-T_0 (K) under the same conditions as in Fig.2, and close-up view around the heater.

5. Normalized velocity from the heater surface to the top wall, under the same conditions as in Fig. 2.

6. Simulated velocity profile, viewed from the symmetry plane (x = 0) under the same conditions as in Fig. 2.

7. (Left) temperature difference T-T_0 (K) and (right) velocity (mm/s) distribution for the 2D analysis and the same operational conditions as in Fig. 2.

8. (a) Zoom view of the velocity distribution (in the symmetry plane, x = 0) showing the symmetric convective cells above the heater; (left) liquid nitrogen and (right) 10 cst silicon oil, under the same injected power as in Fig.2; (b) velocity distribution in the xy plane.

9. Close-up view of the flow distribution above the heater surface for 10 cst silicon oil with a power source density of 9.79 x 10^5 W/m^3; left: present study for mesh M2 and right: PIV measurement.

10. Power law profile for the maximum vertical velocity as a function of ΔT.

11. Dimensionless temperature distribution above the heater surface.

12(a). Schematics of 10.1 cm heater length (due to symmetry, only half of the heater length i.e., 5.05 cm is shown in the figure; the width and heights of the heater are the same as those of the short heater). Here, x = 100 mm, y = 100 mm and z = 30 mm respectively.

12(b). Pathline profiles for 20cst silicon oil with a heater of 10.1cm length and 2 mm diameter for, (top), low input power (0.11W), and, (bottom), high input power (0.61 W). The small and large white circle refers to the cell center and the region of maximum velocity in the xy plane.

13(a). Schematics of 5.7 cm heater length. The magnitude and the directions of length (x), height (y) and the width (z) of the computational domain remains the same as in Fig. 12(a). Due to symmetry plane, only 2.85 cm of the heater length is shown in the figure.

13(b). Characteristics length (λ_c) for 5.7 cm heater length (0.11W input power).

14(a). Variation of the wavelength w.r.t. the input power for the 6mm heater.

14(b). Variation of wavelength w.r.t. input power for the 5.7 cm and 10.1 cm heaters.

15. Maximum vertical velocity as a function of ΔT for extended heater lengths. The maximum velocity is determined in the mid plane x = 0 in both experiments and simulations.

16. Schematic representation of the simulated geometry and definitions of the characteristics lengths λ_c and L.

17. Dimensionless vertical velocity as a function of $(Ra-Ra_c)/Ra_c$ in semi-log scale.

Figure (Appendix A):

18. Top view of the Cryostat [5].

Nomenclature:

Bi	*Biot Number (hL_c/k)*
C_p	*specific heat (J/kg-K)*
g	*acceleration due to gravity (m/s^2)*
H	*domain height*
K	*temperature in Kelvin*
k	*heater thermal conductivity (W/m-K)*
K_f	*fluid thermal conductivity (W/m-K)*
L	*Liquid pool height above the heater (m)*
L_c	*heater Characteristics length*
L_g	*heater lengths*
T_0	*temperature of coolant at rest (K)*
T_h	Temperature of the heater surface
ΔT	$T_h - T_0$*(K)*
q″	*heat generation ($Q/\rho C_p$)*
Q	*volumetric heat source (W/m^3)*
Pr	*Prandtl number*
Ra	*Rayleigh number*
Ra_c	*Critical Rayleigh number*

Greek Symbol

α thermal diffusivity (m^2/s)

β coefficient of thermal expansion ($1/K$)

μ dynamic viscosity ($kg/m\text{-}s$)

ν kinematic viscosity (m^2/s)

ρ density (kg/m^3)

τ_{wall} wall shear stress (kg/ms^2)

Appendix-A: **Thermilization of the Experimental Set-up**

Thermalization of the liquid pool is ensured by immersing the polycarbonate box filled with the studied liquid into a large vessel which is thermalized. In practice, the experimental chamber is placed on small pillars in order to avoid perturbations from eventual bubbles nucleated on the cryostat bottom wall (see Fig. 18).

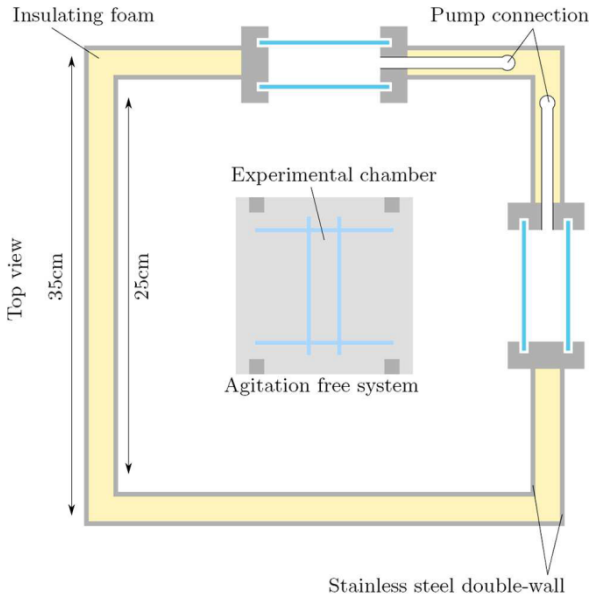

Fig. 18: Top view of the Cryostat [5].

The whole setup is placed on an optical table in order to avoid any vibrations. While the case of silicon oil is rather easy to realize, using liquid nitrogen led us to build a specific cryostat compatible with the PIV technique and allowing large liquid volumes (15 dm^3). Before each experiment, the setup was left at rest a long time enough for the entire liquid to be thermalized.

Appendix-B: **Non-dimensional form of the Governing Equations**

Using the following change of variables;

$$X = \frac{x}{L};\ Y = \frac{y}{L};\ Z = \frac{z}{L};\ U = \frac{uL}{\alpha};\ V = \frac{vL}{\alpha};\ W = \frac{wL}{\alpha};\ \theta = \frac{T - T_0}{\Delta T};\ P = \frac{pL^2}{\rho\alpha^2};\ Ra = \frac{g\beta\Delta TL^3}{\nu\alpha};\ Pr = \frac{\nu}{\alpha}$$

The non-dimensional form of the governing equations (1-5) can be written as;

Continuity:
$$\frac{\partial U}{\partial X} + \frac{\partial V}{\partial Y} + \frac{\partial W}{\partial Z} = 0 \tag{8}$$

x-momentum:
$$U\frac{\partial U}{\partial X} + V\frac{\partial U}{\partial Y} + W\frac{\partial U}{\partial Z} = \frac{-\partial P}{\partial X} + Pr\left(\frac{\partial^2 U}{\partial X^2} + \frac{\partial^2 U}{\partial Y^2} + \frac{\partial^2 U}{\partial Z^2}\right) \tag{9}$$

y-momentum:
$$U\frac{\partial V}{\partial X} + V\frac{\partial V}{\partial Y} + W\frac{\partial W}{\partial Z} = \frac{-\partial P}{\partial Y} + Pr\left(\frac{\partial^2 V}{\partial X^2} + \frac{\partial^2 V}{\partial Y^2} + \frac{\partial^2 V}{\partial Z^2}\right) + RaPr\theta \tag{10}$$

z-momentum:
$$U\frac{\partial W}{\partial X} + V\frac{\partial W}{\partial Y} + W\frac{\partial W}{\partial Z} = \frac{-\partial P}{\partial Z} + Pr\left(\frac{\partial^2 W}{\partial X^2} + \frac{\partial^2 W}{\partial Y^2} + \frac{\partial^2 W}{\partial Z^2}\right) \tag{11}$$

energy:
$$U\frac{\partial \theta}{\partial X} + V\frac{\partial \theta}{\partial Y} + W\frac{\partial \theta}{\partial Z} = \left(\frac{\partial^2 \theta}{\partial X^2} + \frac{\partial^2 \theta}{\partial Y^2} + \frac{\partial^2 \theta}{\partial Z^2}\right) + \frac{Ra^*}{RaPr} \tag{12}$$

where, $Ra^* = \frac{g\beta QL^5}{\alpha^2 k}$; $Ra = \frac{g\beta\Delta TL^3}{\nu\alpha}$, $\Delta T = T_h - T_0$

Boundary Conditions:

- side walls: no-slip velocity i.e., U(X, Y, Z) = 0, V(X, Y, Z) = 0, W(X, Y, Z) = 0 and zero heat flux conditions $\left(\frac{\partial \theta}{\partial X}, \frac{\partial \theta}{\partial Y}, \frac{\partial \theta}{\partial Z}\right) = 0$ are imposed;

- wall attached to the heater surface: symmetry boundary condition i.e., all the normal components of velocity as well as the temperature are zero on the surface (no flux across the boundary);

- Top surface (unfilled part as shown in the Fig. 1): $\theta = \theta_0$, constant temperature is assumed on the top surface with a free-slip velocity condition (shear stress on the wall $\tau_{wall} = 0$);

- a constant volumic heat generation is specified for the heater.

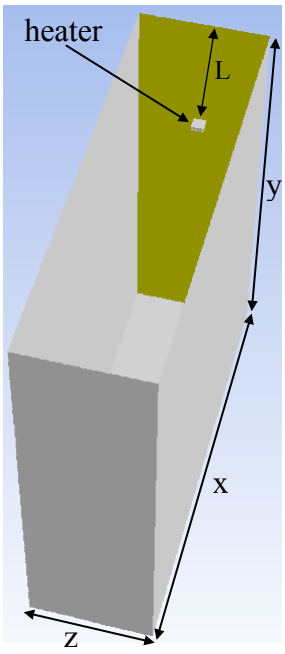

Fig. 1: Schematics of the simulated domain.

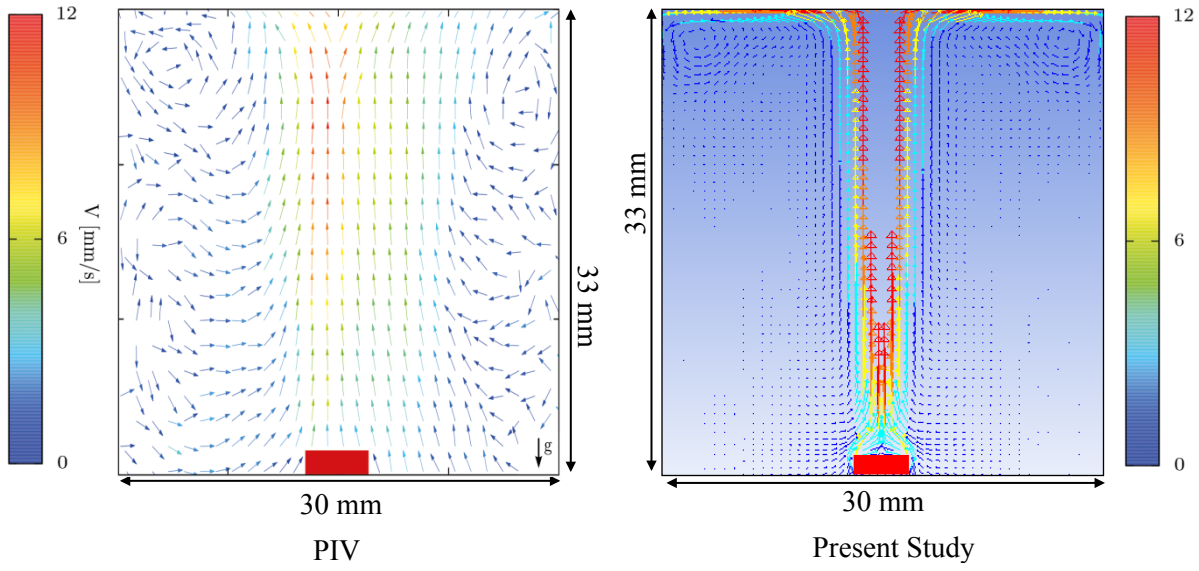

Fig. 2: Close-up view of the flow above the heater surface for the case of liquid nitrogen with a source of power density of 2.2 x 10^6 W/m^3; left: PIV measurement; right: present study for mesh M2. It is noted that, the absence of the velocity vectors in the middle of the present study reflects the higher velocity region up to 22 mm/s.

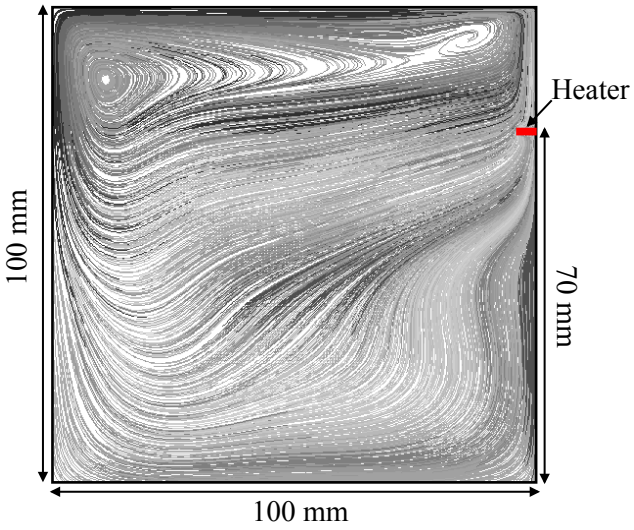

Fig. 3: Path lines colored by individual particle on the mid plane (z = 0), under the same conditions as in Fig. 2 (see above). The fluid is rising above the heater and descends along the container vertical wall.

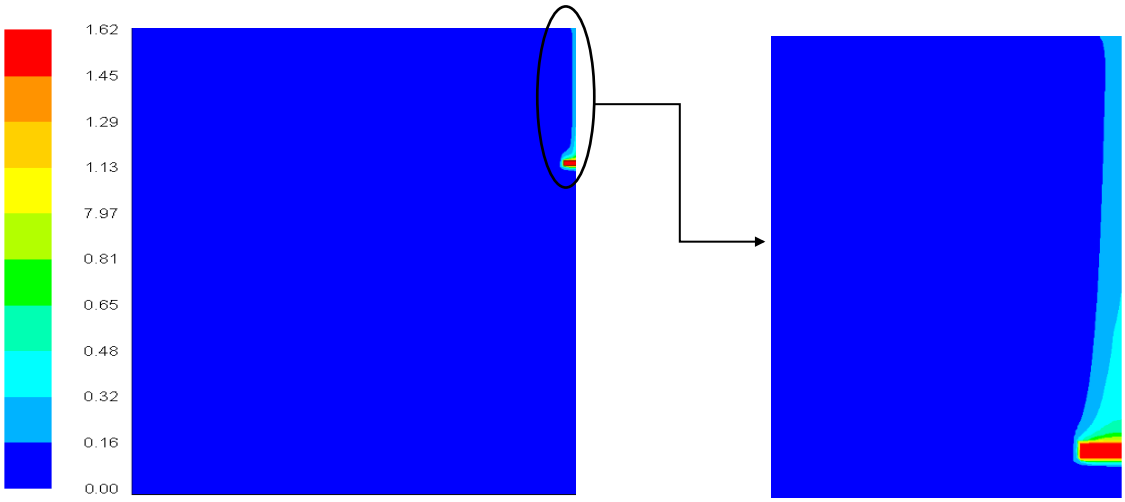

Fig. 4: Distribution of the temperature excess$T$-T_0(K) under the same conditions as in Fig.2, and close-up view around the heater.

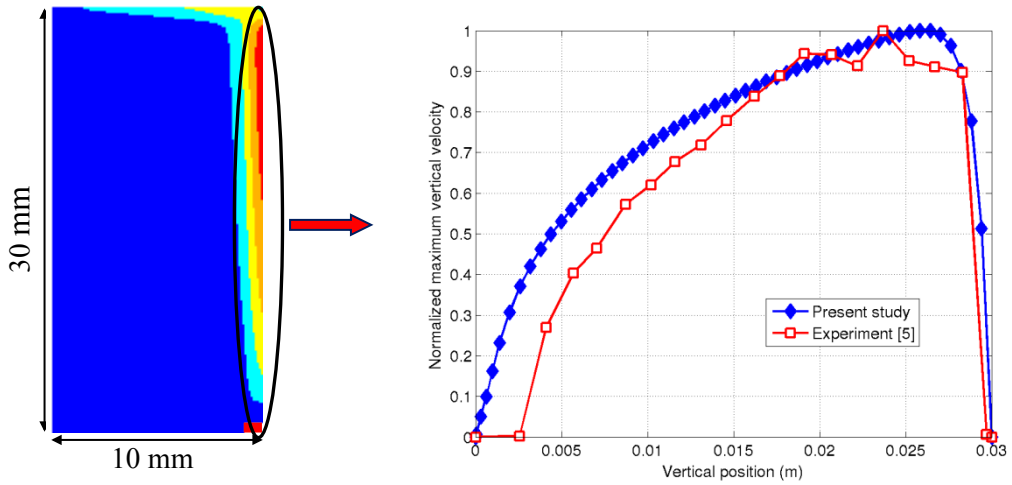

Fig. 5: Normalized velocity from the heater surface to the top wall, under the same conditions as in Fig. 2.

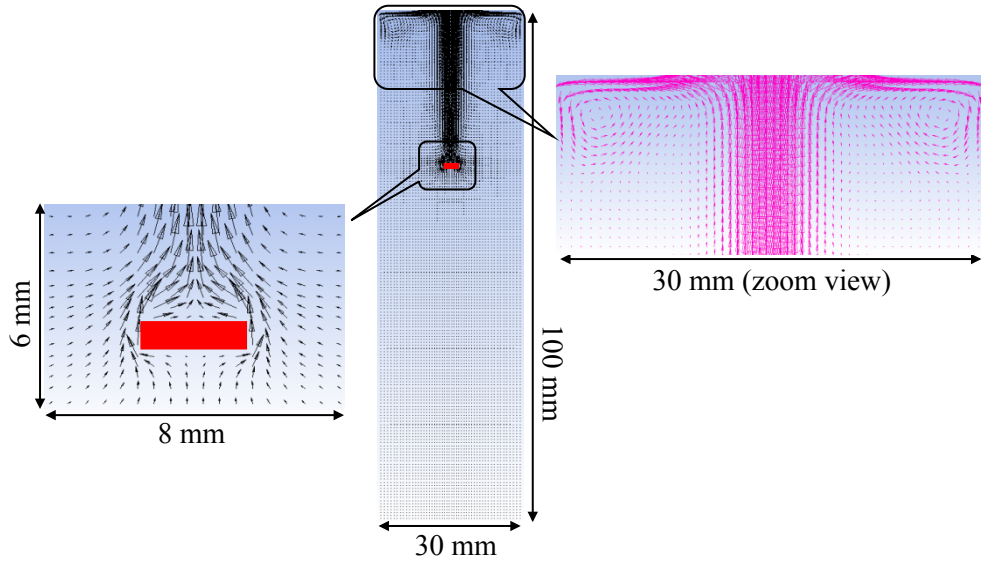

Fig. 6: Simulated velocity profile, viewed from the symmetry plane (yz), (or $x = 0$), under the same conditions as in Fig. 2.

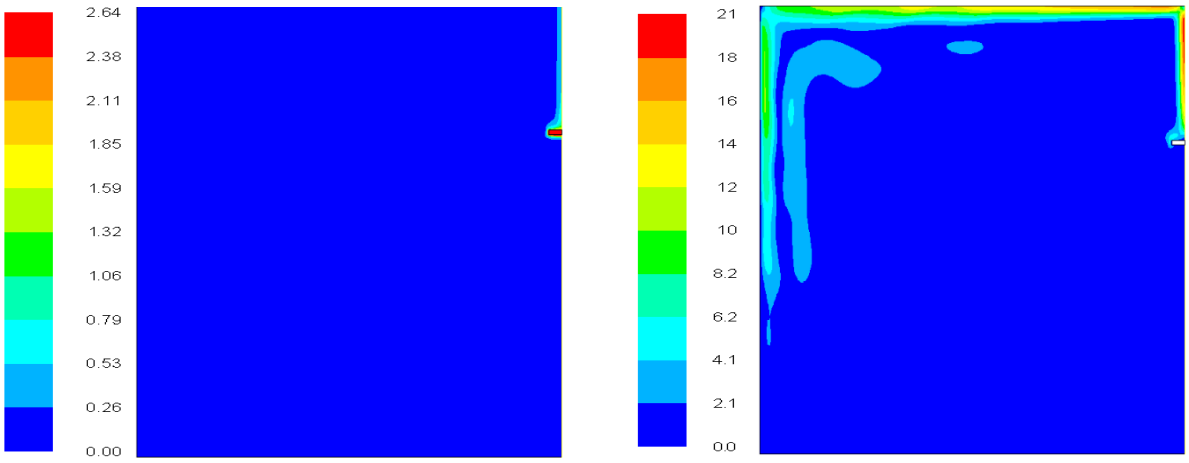

Fig. 7: (left) temperature difference T-T_0(K) and (right) velocity (mm/s) distribution for the 2D analysis and the same operational conditions as in Fig. 2.

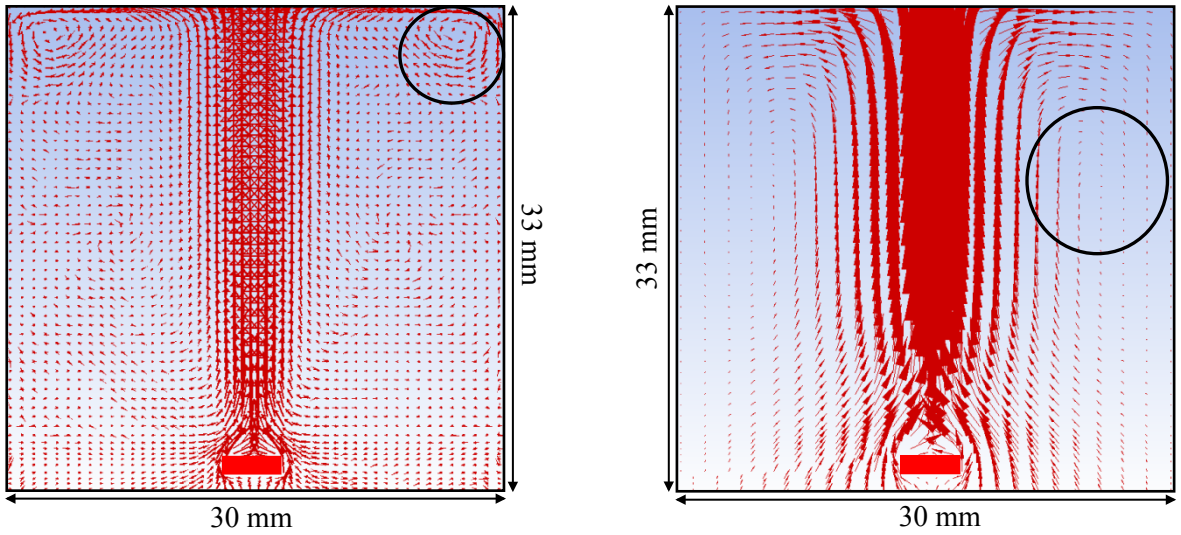

(a)

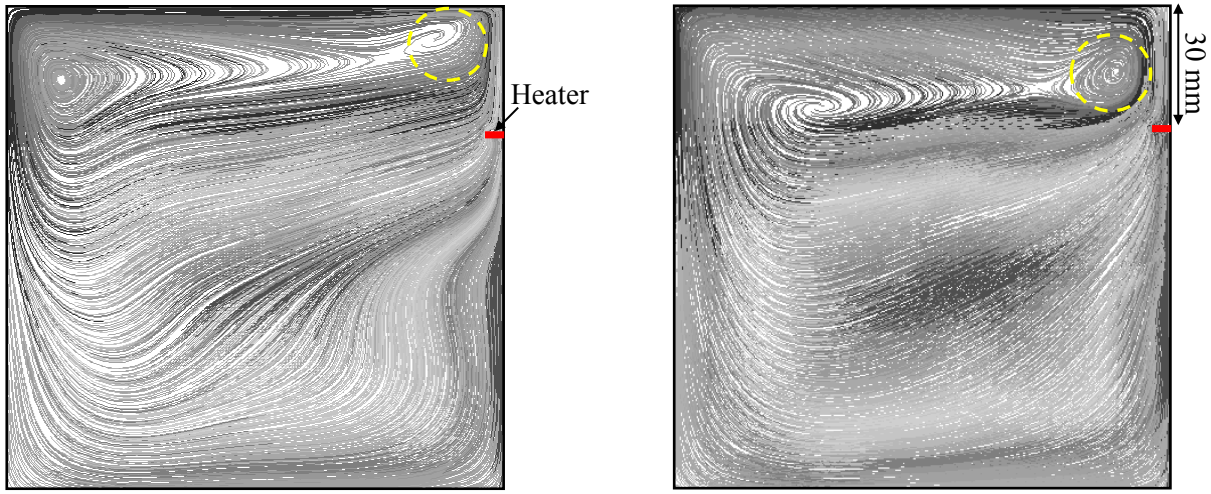

(b)

Fig. 8: (a) Zoom view of the velocity distribution (in the symmetry plane (yz), or (x = 0)) showing the symmetric convective cells above the heater; (left) liquid nitrogen and (right) 10cst silicone oil, under the same injected power as in Fig.2; (b) velocity distribution in the xy plane.

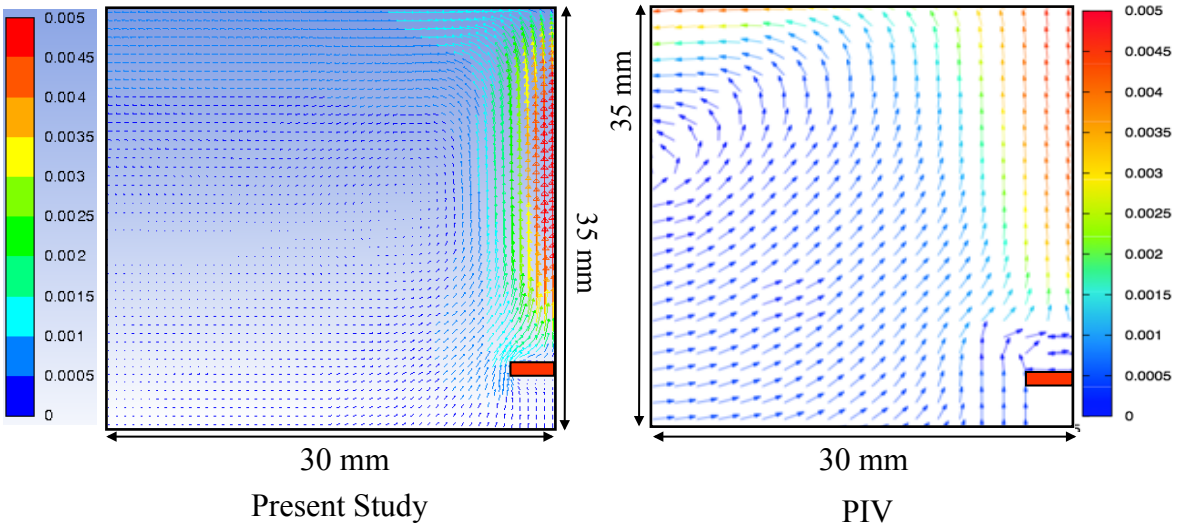

Fig. 9: Close-up view of the flow distribution above the heater surface for 10 cst silicon oil with a power density source of 9.79 x 10^5 W/m^3; left: present study for mesh M2 and right: PIV measurement.

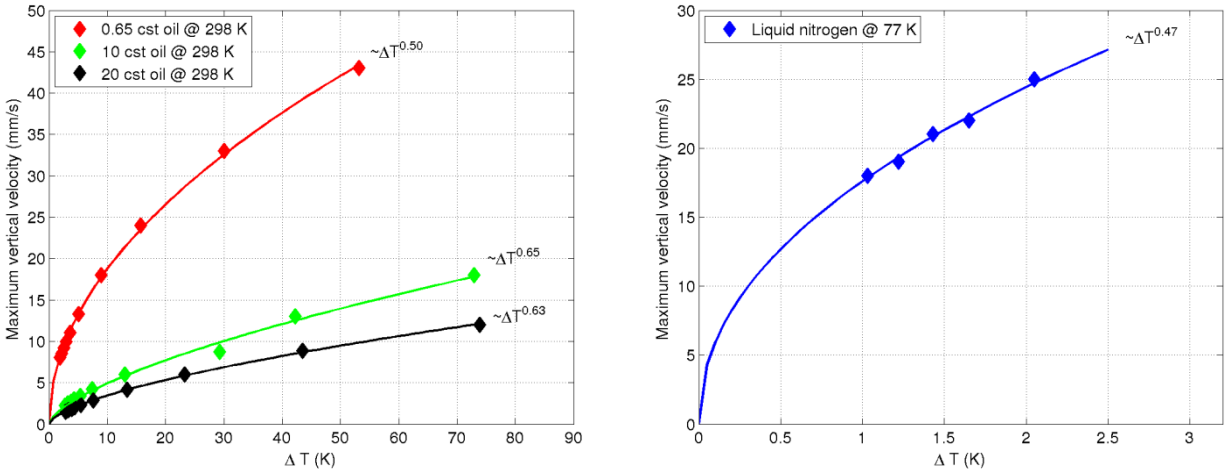

Fig. 10: Power law profile for the maximum vertical velocity as a function of ΔT.

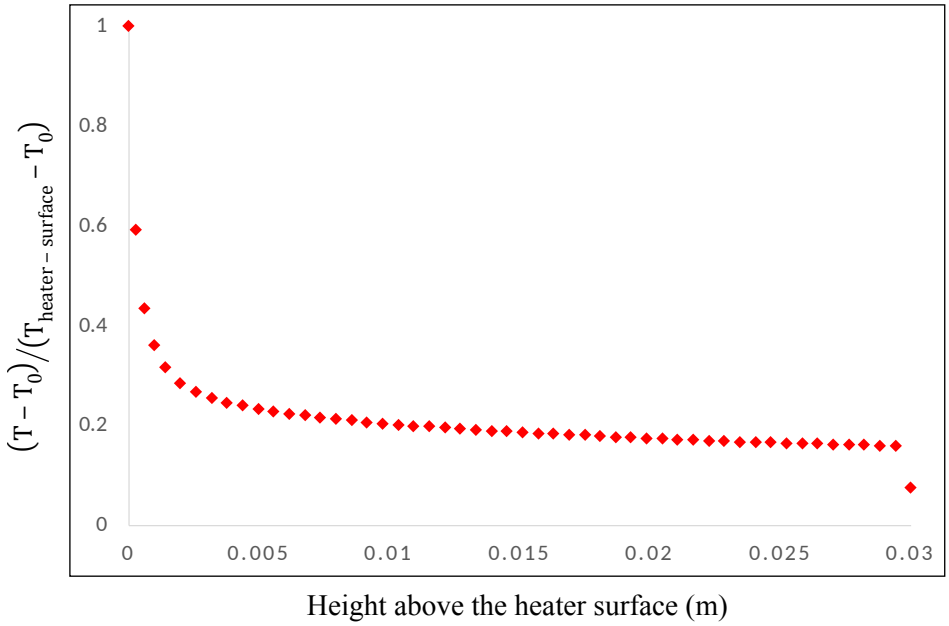

Fig. 11: Dimensionless temperature distribution along the height above the heater surface.

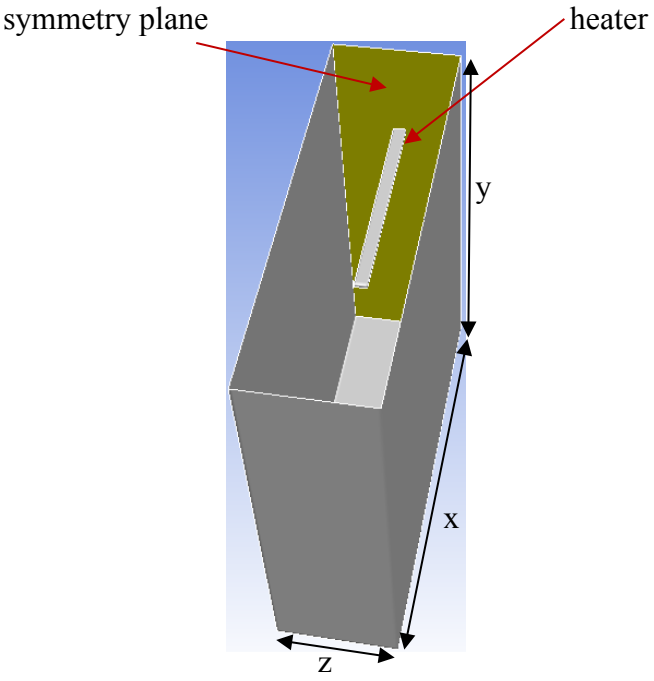

Fig. 12(a) : Schematics of 10.1 cm heater length (due to symmetry, only half of the heater length i.e., 5.05 cm is shown in the figure; the width and heights of the heater are the same as those of the short heater). Here, x = 100 mm, y = 100 mm and z = 30 mm respectivley.

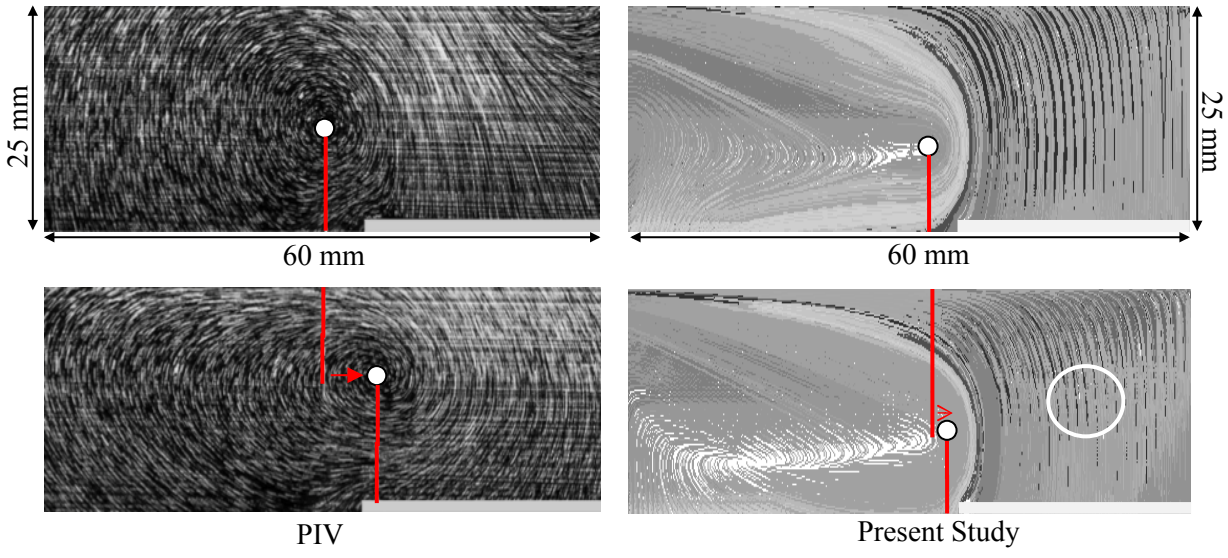

Fig. 12(b) : Pathline profiles for 20cst silicon oil with a heater of 10.1cm length and 2 mm diameter for, (top), low input power (0.11W) and (bottom), high input power (0.61 W). The small and large white circles refer to the cell center and the region of maximum velocity in the xy plane, respectively.

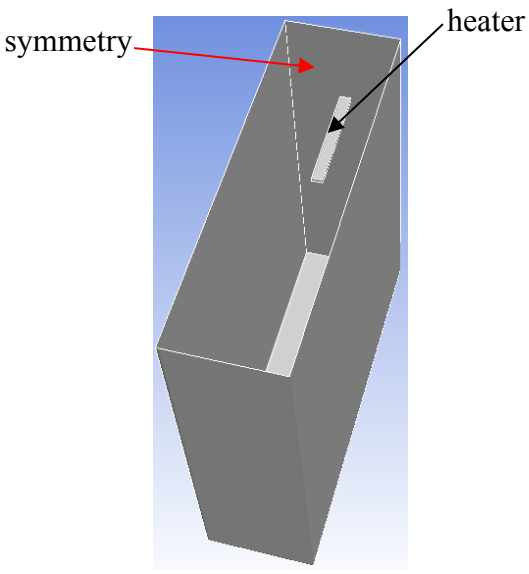

Fig. 13(a) : Schematics of 5.7 cm heater length. The magnitude and the directions of length (x), height (y) and the width (z) of the computational domain remains the same as in Fig. 12(a). Due to symmetry plane, only 2.85 cm of the heater length is shown in the figure.

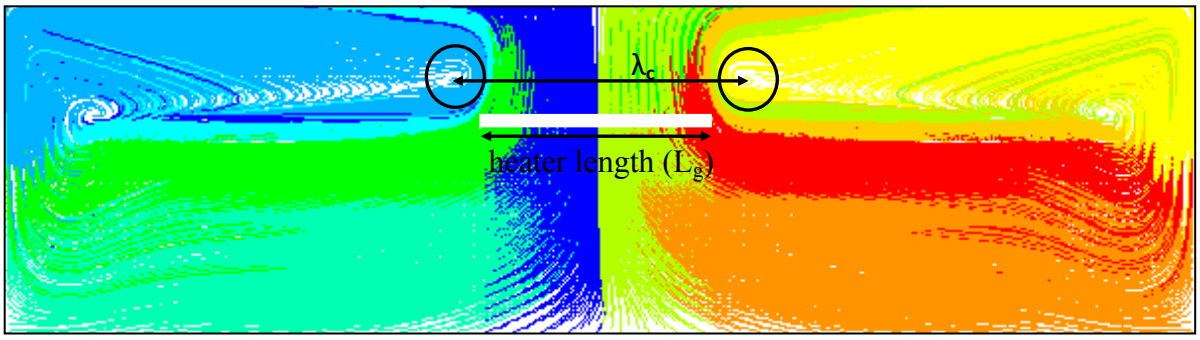

Fig. 13(b): Characteristics length (λ_c) for 5.7 cm heater length (0.11W input power).

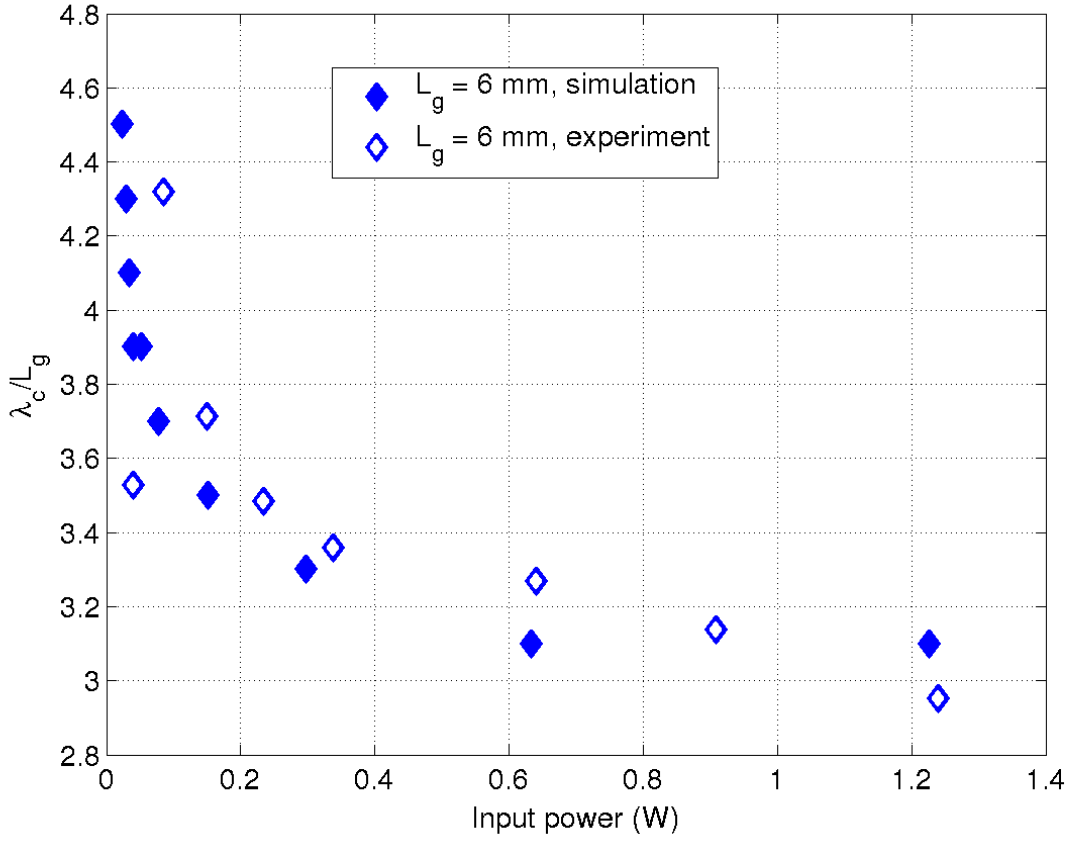

Fig. 14(a): Variation of the wavelength w.r.t. the input power for the 6mm heater.

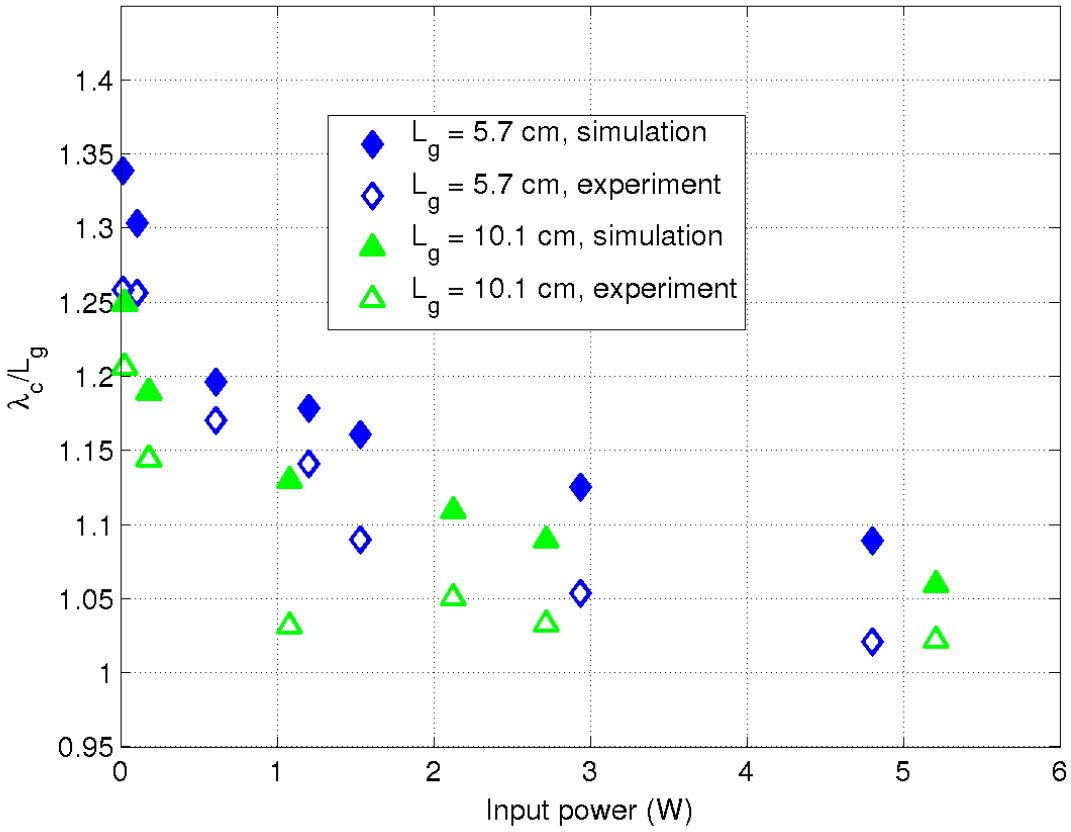

Fig. 14(b): Variation of wavelengthw.r.t. input power for the 5.7 cm and 10.1 cm heaters.

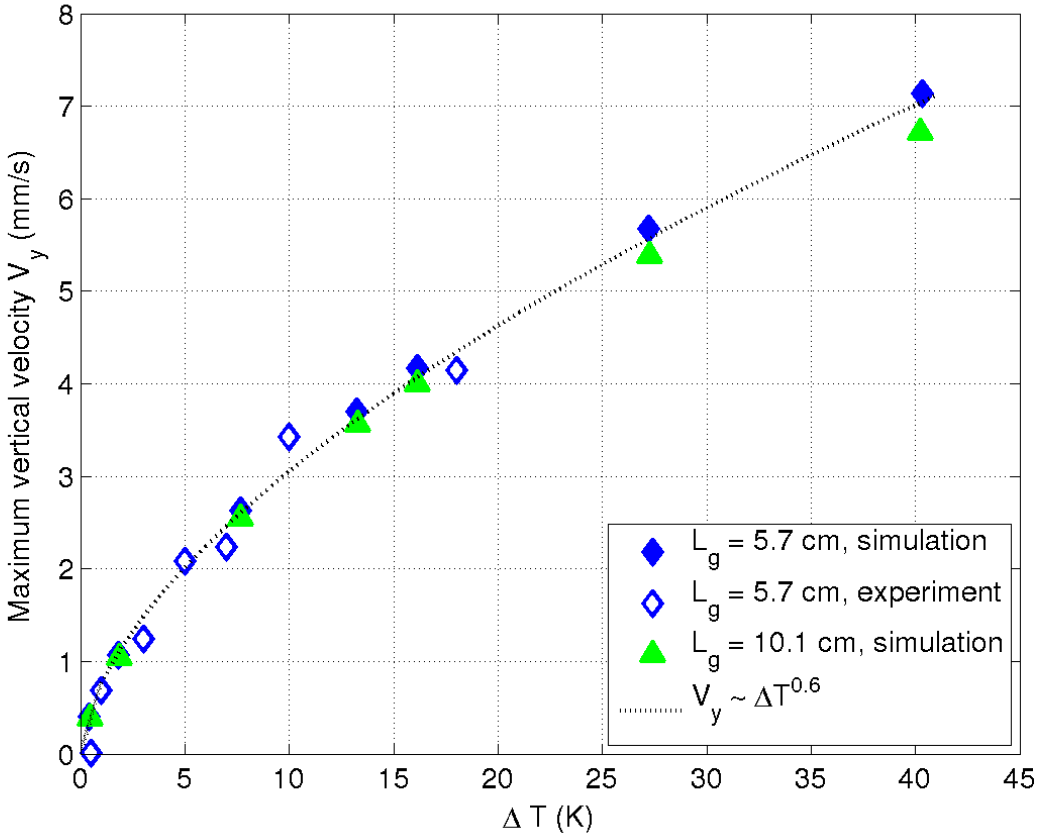

Fig.15: Maximum vertical velocity as a function of ΔT for extended heater lengths. The maximum velocity is determined in the mid plane x = 0 in both experiments and simulations.

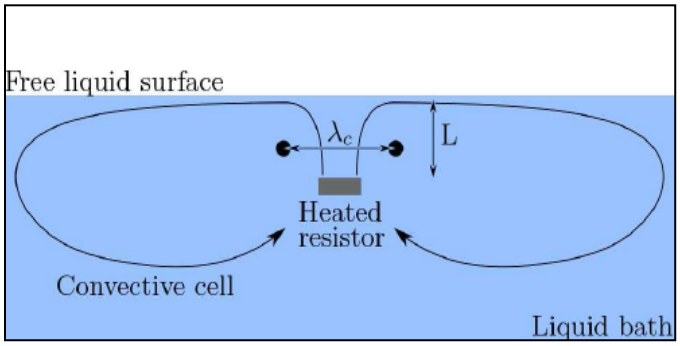

Fig.16: Schematic representation of the simulated geometry and definitions of the characteristics lengths λ_c and L.

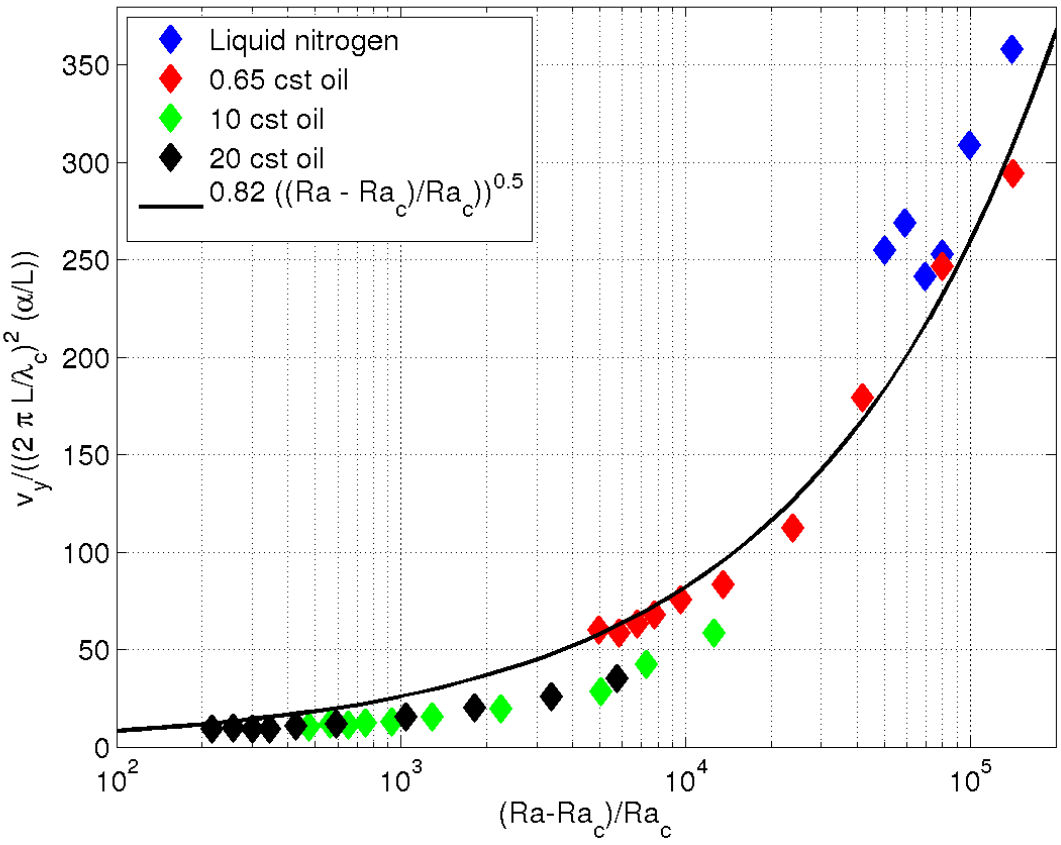

Fig. 17: Dimensionless vertical velocity as a function of $(Ra-Ra_c)/Ra_c$ in semi-log scale.

Table 1: Fluid properties: kinematic viscosity v, density ρ, thermal expansion coefficient β, thermal diffusivity α, thermal conductivity K_f.

Liquid	v (m^2/s)	ρ (kg/m^3)	β (1/K)	α (m^2/s)	K_f (W/m-K)	Pr
Liquid nitrogen (77 K)	2.0E-7	810	5.0E-3	8.0E-8	0.132	2.5
Silicon oil 0.65 cst (298	0.65E-6	905	1.0E-3	9.0E-8	0.12	7.2
Silicon oil 10 cst (298 K)	10E-6	934	1.0E-3	9.0E-8	0.123	111
Silicon oil 20 cst (298 K)	20E-6	950	1.0E-3	1.0E-7	0.14	200

Table 2: Mesh sensitivity study for liquid nitrogen subjected to a 6 mm heater dissipating 2.2×10^6 W/m^3 (40 mW).

Mesh	Total number of control volumes	Height of the first boundary layer from the heater surface with a successive boundary layer growth of 1.1 (m)	Temperature difference ΔT (K)	Maximum vertical velocity (mm/s)	
				1st order	2nd order
M1	789 400	0.0006	2.0	24.0	23.2
M2	1 396 900	0.0003	1.62	22.0	21.3
M3	2 586 020	0.0001	1.58	20.0	19.4
Experiment	-	-	2.0	12	

Table 3: Comparison of the exponent '*m*' for different fluids

Liquid	Power coefficient(*m*)	
	Present Study	Experiment [5]
Liquid Nitrogen (77K)	0.47	0.49
Silicone oil 0.65 cst (298 K)	0.50	0.51
Silicone oil 10 cst (298 K)	0.65	0.53
Silicone oil 20 cst (298 K)	0.63	0.60